Hindawi

Research Article

Vibration Response Analysis of a Tethered Unmanned Aerial Vehicle System under Transient Wind Field

Wei He [ID] **and Suxia Zhang** [ID]

Department of Mechanics, School of Mechanical Engineering, Tianjin University, Tianjin 300354, China

Correspondence should be addressed to Suxia Zhang; zhangsux@tju.edu.cn

The transient wind is one of the dangerous conditions encountered by tethered UAVs operating at the ocean, making the cable and the UAV generate complex nonlinear vibration responses threatening normal operation, even safe flight. There is a lack of research on the nonlinear vibration of the tethered UAV in a transient wind field environment. This study analyzes the vibration response of a tethered quadrotor UAV under a transient wind field, which helps to boost the tethered UAV applications, providing engineering suggestions to design these systems. Considering both cable and UAV motions, the coupled dynamic equations of the tethered UAV system are established based on the Hamilton principle. The variation law of the cable vibration amplitudes with wind field and position is analyzed through a one-minus-cosine gust profile to describe the transient wind field, which can evaluate the dynamic behavior of systems in the actual flight. Moreover, the positions of maximum vibration amplitude in tangential and normal directions are found to be approximately 9/10 and 9/20 from the lower end of the cable. Furthermore, the tethered UAV system vibrations are investigated under different structural parameters. The results indicate that the UAV can maintain a stable single-period motion by increasing the length or elastic modulus or selecting the appropriate diameters of the cable. Finally, an experiment is implemented on the vibration response of the tethered UAV system in a wind tunnel. The theoretical result is compatible with the experimental one, demonstrating the theoretical method's accuracy.

1. Introduction

A tethered unmanned aerial vehicle (UAV) has become a research hotspot due to its long-term flight characteristics. Due to transient wind fast velocity variation [1, 2], the transient wind imposes loads on the UAV and cable when the tethered UAV encounters this transient wind during operation. This generates a complex nonlinear vibration response. Accordingly, the flight control of the system cannot preserve stability, which may lead to instability and even a crash of the UAV. This demonstrates the importance of studying the vibration response characteristics of tethered UAV systems under the transient wind field, which provides a theoretical direction for their flight control and structure.

Various studies have been performed on tethered UAV systems. Li et al. [3] and Muttin [4] employed the finite element method to establish the tethered quadrotor UAV's configuration under an average wind field. Xie [5] investigated the flight control of the tethered quadrotor UAV from take-off to hovering under the average wind. Mfiri et al. [6] designed a control system for automatically landing a tethered quadrotor aircraft under the average wind. Although the flight control of tethered UAVs was analyzed in a hovering state under an average wind field [7, 8], the cable motion was not considered. Rossi et al. [9] developed a two-layer control strategy to realize a safe landing for tethered UAVs on an inclined plane under the transient wind field. Tethered UAV system has been widely utilized in various engineering applications, such as flood control and drought reduction, hydrology and water resource monitoring, water and soil conservation monitoring, river monitoring and supervision, water conservation project monitoring, relay communication, and emergency mapping [10–13]. However, all these studies were mainly performed under the average wind field by focusing on the relevant control algorithm, and there is a lack of research on the dynamic response of the tethered UAV under the transient wind from the mechanical structure perspective.

In addition to tethered UAVs, tethered systems, such as tethered airships and balloons, were studied under the transient wind field. Li and Wang [14] found that the recovery time of the dynamic response of the tethered balloon under the transient wind field was less than 25 s. The dynamic response of the tethered balloon was simulated under the transient wind field using finite element model [15, 16], and the proposed simulation program was employed for the preliminary evaluation of the technical feasibility of the high-altitude tethered platform system. Kang and Lee [17] developed a simulation program to simulate the vibration response of the tethered airship under the transient wind field, which could reasonably predict the system's dynamic behavior, as demonstrated by the statistical data of the cable. The dynamic response analysis of tethered UAV systems, which can evaluate the feasibility of their design and predict the system's dynamic behavior under the transient wind field, is crucial for designing flight control and structure.

This paper analyzes a tethered quadrotor UAV's dynamic response under dangerous conditions at the ocean-transient wind fields. Considering both cable and UAV motions, the Hamilton principle is utilized to derive the coupled dynamic equations of the tethered quadrotor UAV system, and the first two orders of ordinary differential dynamic equations are obtained by discretization and solved numerically. The distribution of the vibration amplitude of the cable with the position is presented. Besides, the system's vibration characteristics are analyzed under different structural parameters, providing engineering suggestions for designing and applying tethered UAVs. Finally, the numerical method is evaluated via an experiment on the vibration response of the tethered UAV system in a wind tunnel. The accuracy of the theoretical method is demonstrated by comparing the numerical results with the experimental ones.

2. Mathematical Model

In order to establish the mathematical models, the forces acting on the cable and UAV under the wind field are analyzed. Then, the partial differential dynamic equations of the tethered UAV system in tangential and normal directions are derived based on the Hamilton principle. Finally, the system's vibration modes are derived. Besides, the system's first two-order ordinary differential dynamic equations in tangential and normal directions are obtained using the Galerkin method. Before the mathematical modeling of the tethered UAV system, the following hypotheses are considered:

(1) A quadrotor UAV is adopted in this paper. Due to its geometric symmetry, only the in-plane motion of the tethered UAV system is considered

(2) This study does not take into account the rotation of the UAV; instead, it operates under the assumption that each rotor contributes an equal amount of lift. In other words, the rotor speed does not fluctuate over time

(3) The photoelectric integrated cable is utilized in the actual project, and the cable's linear density ρ, stiff-

ness EA, and other structural parameters are considered constant. Moreover, the cable's torsion and shear deformation are not considered

(4) The tension point of the cable on the quadrotor UAV is located at the body's center of mass

2.1. Dynamic Equations of the Tethered UAV System

2.1.1. Analysis of Force Acting on the Cable. The schematic diagram of tethered UAV system is shown in Figure 1(a), where V is the wind speed and l is the initial length of the cable. The displacement u of the system is decomposed into components u_1 and u_2 along with the tangential and normal directions e_1 and e_2, respectively. θ^0 and θ represent the angles of the cable between the tangential and horizontal directions in the initial and dynamic configurations R^0 and R^f, respectively. The force diagram of the cable element under the wind field is shown in Figure 1(b). The cable is subject to gravity $\rho g ds$, tension P_T, tangential wind load F_t, and normal wind load F_n. P_T can be expressed as $P_T = P + EA\varepsilon$, where P is the static equilibrium tension [18] and ε is the Lagrangian dynamic strain [19], described as

$$\varepsilon = u_{1,s} - Ku_2 + \frac{1}{2}\left[(u_{1,s} - Ku_2)^2 + (u_{2,s} + Ku_1)^2\right], \quad (1)$$

where K represents the curvature [18]. $_{,s}$, $_{,ss}$, $_{,t}$ and $_{,tt}$ represent $\partial/\partial s$, $\partial^2/\partial s^2$, $\partial/\partial t$, and $\partial^2/\partial t^2$, respectively.

The tethered UAV consists of a cable and a UAV, and the cable and the UAV motion are coupled in practice. Therefore, the kinetic energy Π_k^f, strain energy Π_s^f, gravitational potential energy Π_g^f, and external work Π_f^f of both the cable and the UAV must be considered.

$$\Pi_k^f = \frac{1}{2}\rho\int_0^l \left(u_{1,t}{}^2 + u_{2,t}{}^2\right)ds + \frac{1}{2}m\left[u_{1,t}{}^2(l,t) + u_{2,t}{}^2(l,t)\right], \quad (2)$$

$$\Pi_s^f = \int_0^l \left(P + \frac{1}{2}EA\varepsilon\right)\varepsilon ds, \quad (3)$$

$$\Pi_g^f = \int_0^l \rho g(u_1 \sin\theta + u_2 \cos\theta)ds + mg\sin\theta^0(l)u_1 + mg\cos\theta^0(l)u_2, \quad (4)$$

$$\Pi_f^f = \int_0^l (F_t u_1 + F_n u_2)ds + \left\{F_L \sin\left[\theta^0(l) + \phi\right]\right\}u_1 + \left\{F_L \cos\left[\theta^0(l) + \phi\right]\right\}u_2 + \left\{F_D(l,t)\cos\left[\theta^0(l) + \phi\right]\right\}u_1 - \left\{F_D(l,t)\sin\left[\theta^0(l) + \phi\right]\right\}u_2, \quad (5)$$

where m is the mass of the UAV and F_t and F_n are given as follows [20]:

$$F_t = \frac{1}{2}\rho_f C_{dt}d(V\cos\theta - u_{1,t})\left|V\cos\theta - u_{1,t}\right|, \quad (6)$$

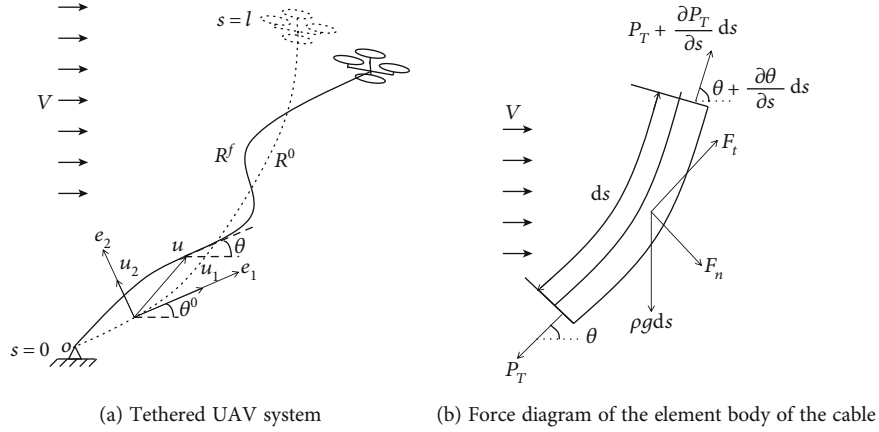(a) Tethered UAV system (b) Force diagram of the element body of the cable

Figure 1: Schematic diagram of the tethered UAV system and the cable element.

$$F_n = \frac{1}{2} \rho_f C_{dn} d(-V \sin \theta - u_{2,t}) |-V \sin \theta - u_{2,t}|, \tag{7}$$

where ρ_f represents the air density, d represents the cable diameter, C_{dt} and C_{dn} indicate the wind resistance coefficients along with the cable's tangential and normal directions, respectively. Since C_{dt} has an order of magnitude smaller than C_{dn} [21], the tangential wind force F_t is neglected in subsequent calculations.

The Hamilton principle is expressed as

$$\delta \int_{t_1}^{t_2} \left(\Pi_k^f - \Pi_s^f - \Pi_g^f + \Pi_f^f \right) dt = 0. \tag{8}$$

Substituting equations (2)–(5) into equation (8), the differential equations of motion of the tethered UAV system can be obtained after derivation as follows [22]:

$$\rho u_{1,tt} = \left[(P + EA\varepsilon)(1 + u_{1,s} - Ku_2) \right]_{,s} \\ - K(P + EA\varepsilon)(u_{2,s} + Ku_1) - \rho g \sin \theta^0 + F_t, \tag{9}$$

$$\rho u_{2,tt} = \left[(P + EA\varepsilon)(u_{2,s} + Ku_1) \right]_{,s} \\ + K(P + EA\varepsilon)(1 + u_{1,s} - Ku_2) - \rho g \cos \theta^0 + F_n. \tag{10}$$

The boundary conditions are

$$s = 0 : u_j = 0, j = 1, 2, \tag{11}$$

$$s = l : mu_{1,tt}(l, t) = F_L \sin \left[\theta^0(l) + \phi \right] - mg \sin \theta^0(l) \\ + F_D \cos \left[\theta^0(l) + \phi \right] - P_T(l, t)[1 + u_{1,s}(l, t) - K(l)u_2(l, t)], \tag{12}$$

$$mu_{2,tt}(l, t) = F_L \cos \left[\theta^0(l) + \phi \right] - mg \cos \theta^0(l) \\ - F_D \sin \left[\theta^0(l) + \phi \right] \tag{13} \\ - P_T(l, t)[u_{2,s}(l, t) + K(l)u_1(l, t)].$$

2.1.2. Analysis of the Forces Acting on a Quadrotor UAV. Figure 2 shows the side view of a quadrotor UAV, which
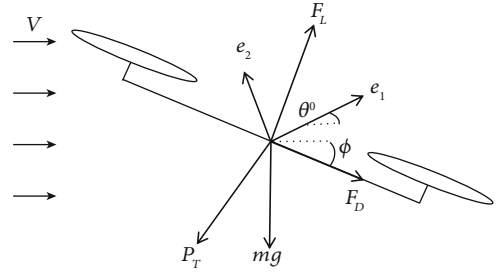

Figure 2: Force diagram of the UAV.

gives the forces acting on the UAV. Under the action of the wind field, the UAV is subject to lift F_L, gravity mg, air resistance F_D, and cable tension P_T, respectively. The UAV's initial pitch angle ϕ is set to maintain the UAV in an initial equilibrium state.

The air resistance F_D of the UAV is expressed as [23]

$$F_D = \frac{1}{2} \rho_f C_D V_D |V_D|, \tag{14}$$

where C_D is the air resistance coefficient of the UAV, and the relative speed V_D between the UAV and the wind is

$$V_D = [V - u_{1,t}(l, t) \cos \theta(l) + u_{2,t}(l, t) \sin \theta(l)] \cos \phi \\ - [u_{1,t}(l, t) \sin \theta(l) + u_{2,t}(l, t) \cos \theta(l)] \sin \phi. \tag{15}$$

The total lift force F_L of a quadrotor UAV generated by four rotors can be obtained as follows [24, 25]:

$$F_L = \sum_{i=1}^{4} 2\rho_f A \sqrt{\frac{k_1 \Omega_i^2}{2\rho_f A}} \sqrt{V^2 + \frac{k_1 \Omega_i^2}{2\rho_f A} - 2V \sqrt{\frac{k_1 \Omega_i^2}{2\rho_f A}} \sin \phi}, \tag{16}$$

where A is the propeller's projected area, k_1 is the lift coefficient, and Ω_i is the rotational speed of the ith rotor.

2.2. Discrete Dynamic Model of the Tethered UAV System.
The Galerkin method [26] discretizes the system dynamics (equations (9)–(13)). Scholars indicated that the first two modes have an order of magnitude larger than the third- or higher-order ones [27, 28]. Therefore, only the first two modes are considered in the tangential and normal displacements of the system. The tangential and normal displacements are assumed based on the Galerkin method:

$$u_1 = q_{11} U_{11} + q_{12} U_{12}, \tag{17}$$

$$u_2 = q_{21} U_{21} + q_{22} U_{22}, \tag{18}$$

where q_{11} and q_{12} represent the first two-order displacements, U_{11} and U_{12} describe the first two modes in the tangential direction, q_{21} and q_{22} represent the first two-order displacements, and U_{21} and U_{22} are the first two modes in the normal direction.

Only the linear part and free vibration are required when calculating the vibration mode function of the system. Thus, the external excitation and nonlinear terms versus u_1 and u_2 in equations (2)–(6) are removed, and the resulting equations are expressed in the following matrix form:

$$A_1 x_{,tt} = B x_{,ss} + C x_{,s} + D x. \tag{19}$$

Boundary conditions are described as follows:

$$s = 0 : x = 0, \tag{20}$$

$$s = l : A_2 x_{,tt} = G x_{,s} + H x, \tag{21}$$

where

$$
\begin{aligned}
A_1 &= \begin{bmatrix} \rho & 0 \\ 0 & \rho \end{bmatrix}, \\[6pt]
A_2 &= \begin{bmatrix} m & 0 \\ 0 & m \end{bmatrix}, \\[6pt]
B &= \begin{bmatrix} P + EA & 0 \\ 0 & P \end{bmatrix}, \\[6pt]
C &= \begin{bmatrix} P_{,s} & -(EAK + 2PK) \\ 2PK + EAK & P_{,s} \end{bmatrix}, \\[6pt]
D &= \begin{bmatrix} -PK^2 & -(PK_{,s} + P_{,s}K + EAK_{,s}) \\ PK_{,s} + KP_{,s} & -(EAK^2 + PK^2) \end{bmatrix}, \\[6pt]
G &= \begin{bmatrix} -(EA + P) & 0 \\ 0 & -P \end{bmatrix}, \\[6pt]
H &= \begin{bmatrix} 0 & EAK + PK \\ -PK & 0 \end{bmatrix}, \\[6pt]
x &= \begin{bmatrix} u_1 \\ u_2 \end{bmatrix}.
\end{aligned}
\tag{22}
$$

$x_{,tt}$, $x_{,ss}$, and $x_{,s}$ represent $\partial^2 x / \partial t^2$, $\partial^2 x / \partial s^2$, and $\partial x / \partial s$, respectively.

Since equation (19) is a wave equation, the vibration mode is expressed as $U(s) = A_0 \sin((p/a)s) + B_0 \cos((p/a)s)$, where

$$p = \begin{bmatrix} p_t \\ p_n \end{bmatrix}, \tag{23}$$

and p_t and p_n represent the system's tangential and normal circular frequencies, respectively. A_0 and B_0 represent the general solution coefficients. Substituting the vibration mode into the boundary conditions (20) and (21) gives the following frequency equation:

$$\frac{Gp}{A_2 a} + \left(\frac{H}{A_2} + \frac{p^2}{a^2}\right) \tan\left(\frac{p}{a} l\right) = 0. \tag{24}$$

Then, by setting $\beta = pl/a$, the frequency equation (24) can be rewritten as

$$\frac{G\beta}{A_2 l} + \left(\frac{H}{A_2} + \frac{\beta^2}{l^2}\right) \tan(\beta) = 0. \tag{25}$$

The transcendental equation (25) is solved using the least-squares method to obtain the first two-order vibration mode of the system. The system's first two-order ordinary differential equations in the tangential and normal directions can be obtained by substituting equations (17) and (18) into equations (9)–(13) and integrating from 0 to l.

3. Analysis of Vibration Responses of a Tethered UAV System under Transient Wind Field

3.1. The Variation Law of the Cable Amplitude with the Wind Field's Peak Velocities, Periods, and Positions. The tethered UAV is assumed to work in the Bohai region, the transient wind is dangerous at the ocean, where the average wind velocity is 5~7 m/s and reaches the whole gale [29]. Various models of transient wind are available in engineering simulations [30]. The actual measurement curve of ocean wind is shown in Figure 3 [31]; the one-minus-cosine gust profile is closest to the ocean wind curve. Therefore, this study uses a one-minus-cosine gust profile to describe transient wind, as shown in equation (26).

$$V = \frac{V_A}{2} \left[1 - \cos\left(2\pi \frac{t}{T}\right)\right] \quad 0 \le t \le T, \tag{26}$$

where V_A and T represent the wind field amplitude and period, respectively.

This paper focuses on the dynamic response in one feedback loop of the flight control in which the active control does not work; that is, the rotor's rotational speed remains constant. The average wind velocity is chosen as $\bar{V} = 5$ m/s, and the transient wind field's amplitudes and periods are
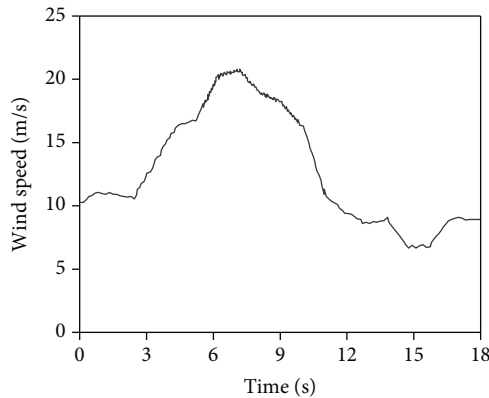
FIGURE 3: The actual measurement curve of ocean wind [31].

$V_A = 0 \sim 20$ m/s and $T = 0 \sim 5$ s, respectively. Table 1 shows the specific parameters of the tethered UAV system [32].

In the following, the variation of cable amplitude under a transient wind field with different peak velocities and periods is analyzed. By setting $T = 1$ s and $V_A = 0 \sim 20$ m/s, the fourth-order Runge-Kutta method with a time step of 0.0025 s is utilized to solve equation (18) numerically. Figure 4 shows the contours for motion amplitudes of the cable in tangential and normal directions, relating to V_A and position s. Figure 4(a) shows that the contour lines become increasingly curved as V_A gradually increases. For example, a vertical dashed line is drawn at any point where $V_A = 12$ m/s, which intersects the contour line with a tangential amplitude of 4.362 m at $s = 200$ m and $s = 152$ m, indicating that the cable has the same tangential motion amplitude at $s = 200$ m and $s = 152$ m when $V_A = 12$ m/s. Besides, it is found that the contour line with tangential amplitude less than 0.250 m has only one intersection point with any vertical dashed line, indicating that different cable positions have different amplitudes. A vertical solid line is drawn tangent to the contour line with a tangential amplitude of 0.250 m, where its abscissa is $V_A = 0.66$ m/s. The tangential motion amplitudes of two cable positions are equal when V_A is between 0.66 m/s and 20 m/s. As shown in Figure 4(b), as V_A increases, the contour line gradually changes from the shape of "2" to the shape of "C." Among them, contour lines with normal amplitudes less than 8.752 m presented the shape of "2" and have three intersection points with any vertical dashed line, indicating that the normal motion amplitudes of the cable at three positions are equal. Contour lines with normal amplitudes greater than 8.752 m show the shape of "C" and have two intersection points with any vertical dashed line, indicating that the normal motion amplitudes of the cable at the two positions are equal. A vertical solid line is drawn tangent to the contour line with a normal amplitude of 8.752 m, where its abscissa is $V_A = 15.2$ m/s. The three positions of the cable have the same normal motion amplitudes when $V_A = 0 \sim 15.2$ m/s. When $V_A = 15.2 \sim 20$ m/s, the two positions of the cable have the same normal motion amplitudes.

Then, the contours for motion amplitudes of the cable in tangential and normal directions are obtained by setting $V_A = 3$ m/s and $T = 0 \sim 5$ s, relating to T and position s, as

shown in Figure 5. Figure 5(a) shows different tangential amplitudes at all cable positions with T less than 0.065 s. When $T = 0.065 \sim 5$ s, the contour line in this region has two intersection points with any vertical dashed line; that is, the two cable positions have the same tangential motion amplitudes. In Figure 5(b), contour lines are in the shape of "2" in the whole region of $T = 0 \sim 5$ s, and there are three intersection points with any vertical dashed line; that is, the three cable positions have the same normal motion amplitudes.

Figures 4 and 5 show that as V_A and T vary, the cable's amplitudes at different positions are the same. The dynamic behavior of the cable in the actual flight can be preliminarily evaluated and premeasured according to the variation law of the cable amplitude with V_A, T, and position s described above.

Besides, Figure 4 shows that the tangential and normal amplitudes of the cable increase with the increase of V_A, and the positions with maximum amplitude in tangential and normal directions are approximately at 9/10 and 9/20 from the lower end of the cable, respectively. As shown in Figure 5, the cable's tangential and normal amplitudes are maximized when $T = 2.75$ s. The positions of maximum amplitude in tangential and normal directions are also approximately at 9/10 and 9/20 from the lower end of the cable, respectively. In practical applications, installing vibration absorbers at the positions of the maximum amplitude enables the vibration absorbers to absorb the most energy and thus reduce the vibration.

3.2. System Vibration Analysis of Different Structural Parameters under Transient Wind Field.
The system exhibits different vibrations under different structural parameters. In order to determine the appropriate structural parameters conducive to flight control, the system's vibration is investigated under different structural parameters while making this study generalizable. The structural parameters for analysis are the cable's length, diameter, and elastic modulus. The wind field amplitude and period of the transient wind field are set as 6 m/s and 6 s, respectively, in order to simulate the vibration response of the system under different structural parameters and put forward the design suggestions of the tethered UAV in engineering practice, thus improving the movement stability.

3.2.1. System Vibration Analysis under Different Cable Lengths

(1) System Motion under Different Cable Lengths. In order to verify the system vibration under different cable lengths, the time history of tension at the upper endpoint of the cable and UAV tangential and normal displacements for cable lengths of 120 m, 160 m, 200 m, and 240 m are plotted and the spectrum curves are obtained after applying the Fourier transform, as shown in Figures 6–8, respectively. The cable tension frequency components in Figure 6(b) are similar to those of the UAV tangential motion in Figure 7(b) at each cable length. The cable tension is along with the tangential direction of the UAV, which makes the cable tension

TABLE 1: The tethered UAV system parameters.

Parameter and symbol	Value and unit	Parameter and symbol	Value and unit
The linear density of the cable ρ	0.0125 kg/m	Cable elastic modulus E	1.867×10^9 N/m^2
Wind resistance coefficient along with the cable's normal direction C_{dn}	1.2	Cable diameter d	0.0034 m
Cable length l	200 m	Air density ρ_f	1.29 kg/m^3
UAV's mass m	5.8 kg	Lift coefficient K_1	$6.134 \times 10^{(-5)}$
The projected area of the propeller A	0.129 m^2	The rotational speed of the rotor Ω_i	482 rad/s
Air resistance coefficient of UAV C_D	0.064	Pitch angle ϕ	5°
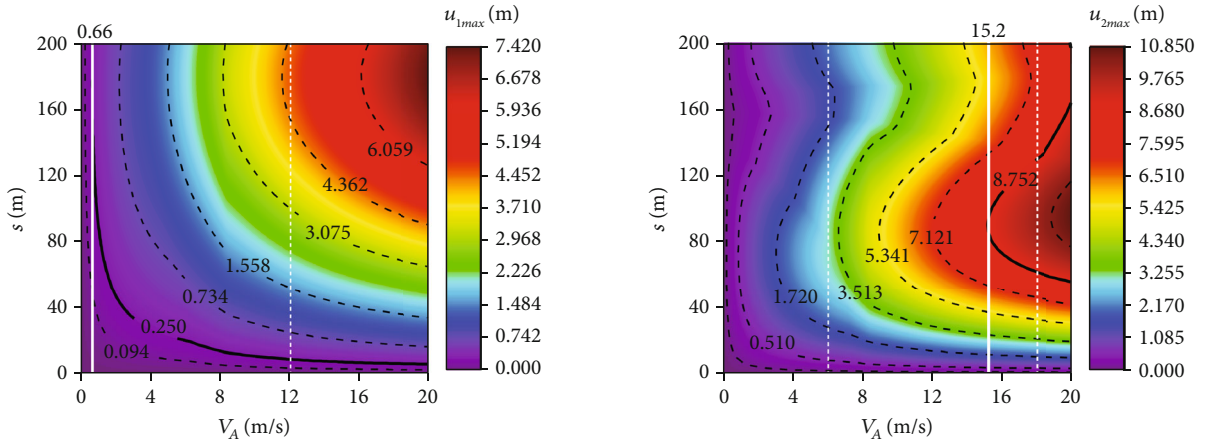
(a) Tangential amplitude of the cable under different wind peak velocities   (b) Normal amplitude of the cable under different wind peak velocities

FIGURE 4: Amplitude distribution of the cable under different wind peak velocities.
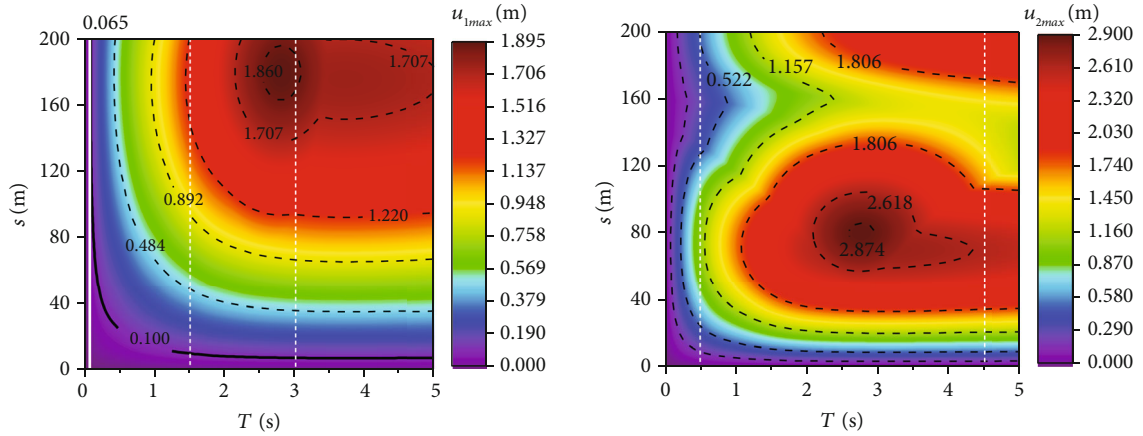
(a) Tangential amplitude of the cable under different wind periods   (b) Normal amplitude of the cable under different wind periods

FIGURE 5: Amplitude distribution of the cable under different wind periods.

predominantly coupled with the UAV tangential motion, causing both to move with the same frequency components. Besides, it can be seen that the frequency doubling amplitude of the cable tension is much smaller than the fundamental frequency amplitude at each cable length. Thus, the frequency doubling component does not make the cable generate evident nonlinear characteristics, and the cable tension time history exhibits a periodic motion.

As shown in Figure 7(a), the tangential displacement variation of the UAV has a periodic motion when the cable length is 160 m, 200 m, and 240 m. When the cable length is 120 m, 160 m, and 200 m, the displacement jumps at the crest and trough, making the UAV motion generate the frequency doubling components. The tangential displacement spectrum curve in Figure 7(b) shows that when the cable length is 120 m, the UAV has three tangential motion frequencies,
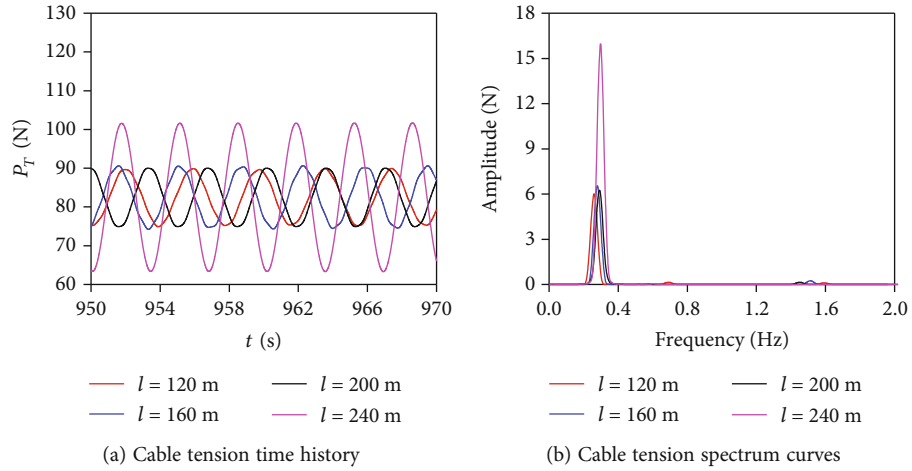
(a) Cable tension time history

(b) Cable tension spectrum curves

FIGURE 6: Tension time history and spectrum curves of the upper end of cable under different cable lengths.

(a) Tangential displacement time history
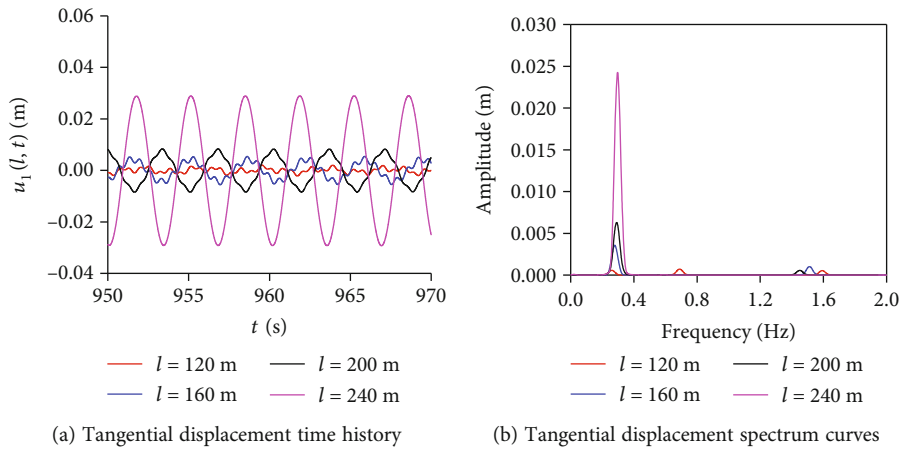
(b) Tangential displacement spectrum curves

FIGURE 7: Tangential displacement time history and spectrum curves of the UAV under different cable lengths.

(a) Normal displacement time history
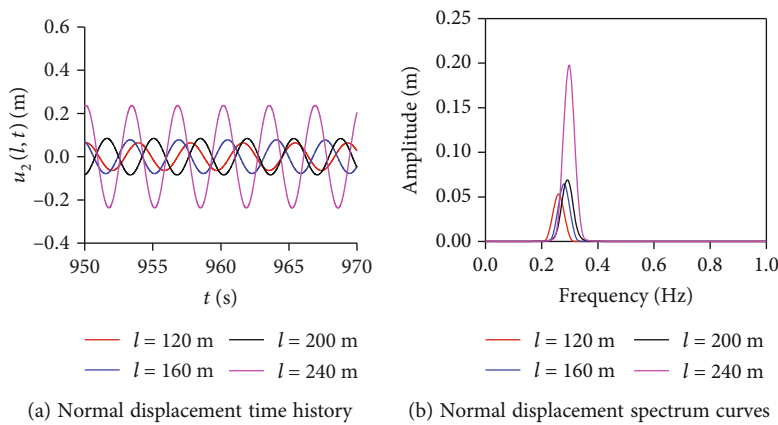
(b) Normal displacement spectrum curves

FIGURE 8: Normal displacement time history and spectrum curves of the UAV under different cable lengths.

including a 0.260 Hz first-order natural frequency, a 0.659 Hz second-order natural frequency, and a 1.595 Hz 6-fold frequency. The amplitude of the frequency doubling component is 98.214% of that of the fundamental component, preventing the UAV from exhibiting stable periodic

vibrations. When the cable length is 160 m, the UAV has two tangential motion frequencies: a 0.279 Hz first-order natural frequency and a 1.517 Hz 27/5-fold frequency, where the amplitude of the frequency doubling component is 29.855% of that of the fundamental component. When the

(a) The tangential displacement of the UAV

(b) Local enlargement of (a)
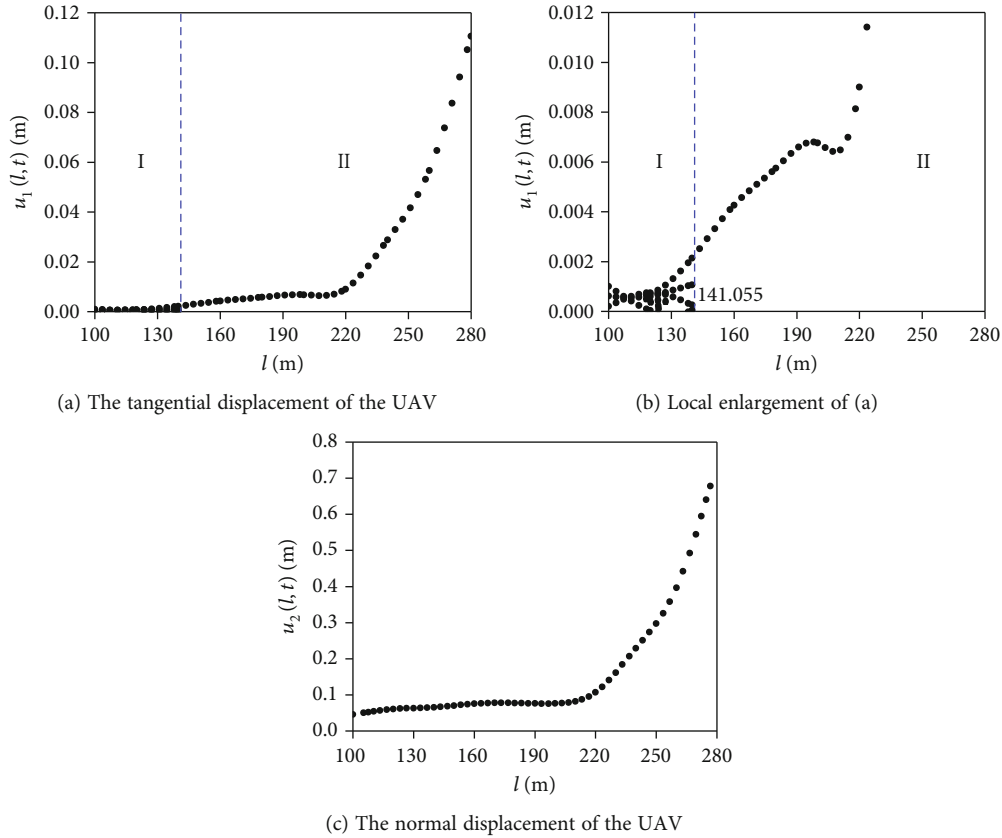

(c) The normal displacement of the UAV

FIGURE 9: Displacement of UAV under different cable lengths.

cable length is 200 m, the UAV has two tangential motion frequencies: a 0.292 Hz first-order natural frequency and a 1.460 Hz 5-octave frequency, where the amplitude of the frequency doubling component is 9.763% of that of the fundamental component. When the cable length is 240 m, there is only a 0.298 Hz first-order natural frequency. The above analysis indicates that as the cable length increases, the first-order natural frequency of the tangential motion of the UAV gradually increases, the tangential second-order natural frequency gradually disappears, and the frequency doubling component decreases until it disappears, thus weakening and disappearing the influence of frequency doubling component gradually. The UAV changes from the first two orders of motion to only a first-order single-periodic stable motion. In the structural design of the tethered UAV system, the cable length can be increased to improve the UAV's motion stability.

Besides, the normal displacement variation of the UAV in Figure 8(a) indicates the periodic trend of the normal displacement curves for different cable lengths. As shown in Figure 8(b), the UAV normal motion only has the first-order natural frequencies of 0.259 Hz, 0.279 Hz, 0.285 Hz, and 0.299 Hz when the cable length is 120 m, 160 m, 200 m, and 240 m, respectively, reflecting the first-order motion of the UAV in the normal direction. Moreover, the natural frequency of the normal motion of the UAV increases gradually as the length of the cable increases. This is due to the increase in the cable length, increasing the static

equilibrium tension, thereby increasing the natural frequency of the UAV. Besides, the tangential natural frequencies of Figure 7(b) are similar to the normal natural frequencies of Figure 8(b), demonstrating the coupling between tangential and normal motions of the UAV.

(2) UAV Motion under Different Cable Lengths. The UAV's motion is the main concern when designing the flight control of the tethered UAV. The motion of the UAV under different cable lengths is presented to provide a theoretical reference for the flight control design. Figure 9 shows the UAV displacement when the cable length varies from 100 m to 280 m. As shown in Figure 9, changing the cable length generates different motion states of the UAV. Figure 9(a) shows the tangential displacement of the UAV when the cable length varies from 100 m to 141.055 m; i.e., the UAV motion in region I generates multiple periodic solutions. The local enlargement in Figure 9(b) shows that the shorter the cable length is, the more periodic solutions appear. In contrast, the UAV motion in region II has one periodic solution when the cable length varies from 141.055 m to 280 m. The normal displacement of the UAV in Figure 9(c) indicates only one periodic solution for the UAV motion in the whole range of cable length change.

The tangential and normal motion phase diagrams of the UAV are then plotted by selecting the cable lengths of 120 m in region I, as shown in Figure 10. Since the tangential phase
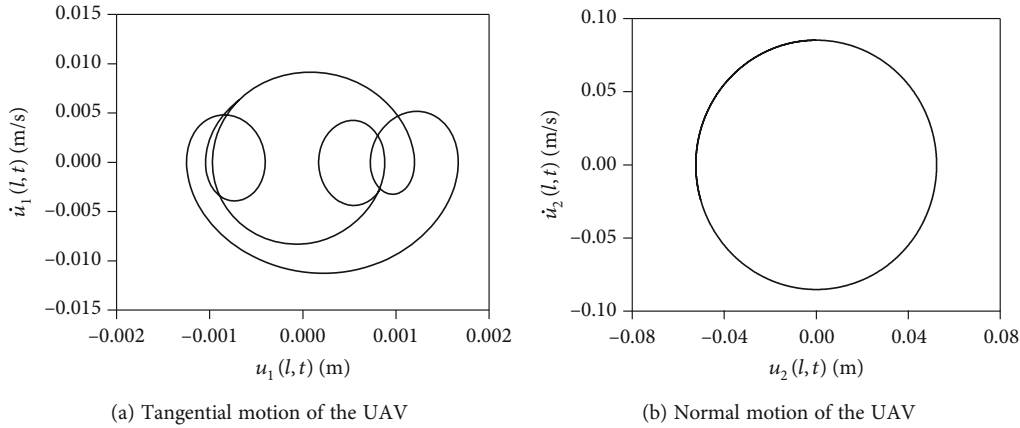
(a) Tangential motion of the UAV

(b) Normal motion of the UAV

FIGURE 10: UAV's motion for $l = 120$ m.

(a) Cable tension time history

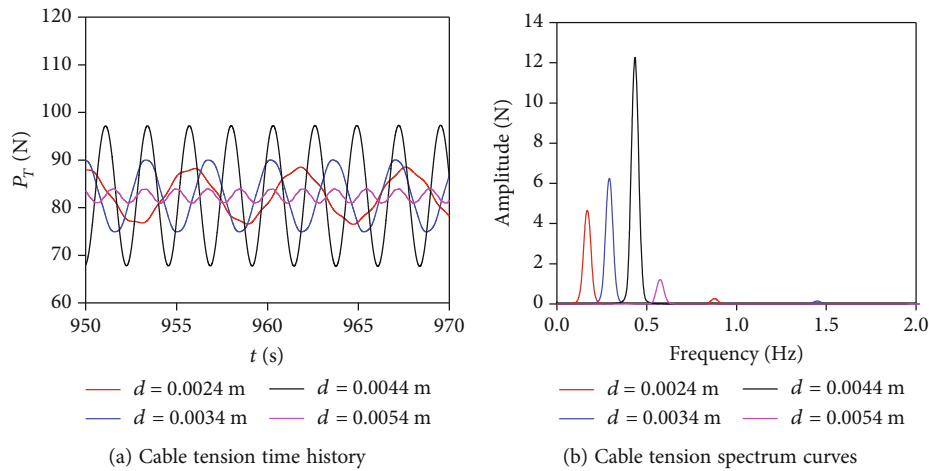(b) Cable tension spectrum curves

FIGURE 11: Tension time history and spectrum curves of the upper end of cable under different cable diameters.

trajectory curve comprises multiple limit loops, the tangential motion of the UAV generates multiple periodic solutions and a multiperiodic motion. The normal phase trajectory curve is a single-limit loop, making the normal motion of the UAV generate only one periodic solution. At the same time, the UAV is in single-period stable motion in the normal direction.

3.2.2. Vibration Analysis of the System under Different Cable Diameters

(1) System Motion under Different Cable Diameters. In order to investigate the system vibration under different cable diameters, the time history of the tension at the upper endpoint of the cable, the tangential and normal displacements of the UAV for cable diameters of 0.0024 m, 0.0034 m, 0.0044 m, and 0.0054 m, and the spectrum curves after applying the Fourier transform are plotted in Figures 11–13, respectively. As shown in Figure 11(a), the cable tension shows periodic motion. As shown in Figure 11(b), when the cable diameter is 0.0034 m, 0.0044 m, and 0.0054 m, the frequency components of the cable tension are similar to those of the tangential motion of the UAV in Figure 12(b), where a

fundamental frequency and an octave frequency exist for the cable diameters of 0.0034 m and 0.0044 m, while the amplitude of the frequency doubling component is much smaller than that of the fundamental frequency component. The cable tension has a fundamental frequency for the cable diameter of 0.0054 m. When the cable diameter is 0.0024 m, the cable tension has only one fundamental frequency, one octave less than the UAV tangential motion frequency. This indicates that the frequency doubling component of the UAV's tangential motion does not affect the cable tension.

The UAV tangential displacement in Figure 12(a) shows a periodic motion. As shown in Figure 12(b), when the cable diameter is 0.0024 m, the tangential motion of the UAV has three frequencies, including the first-order natural frequency of 0.169 Hz, the second-order natural frequency of 0.406 Hz, and the 5-fold frequency of 0.880 Hz, where the amplitude of the 5-fold frequency is 629.120% of that of the second-order natural frequency, demonstrating a significant nonlinear effect of the frequency doubling component on the UAV motion. When the cable diameter is 0.0034 m, the tangential motion of the UAV has two frequencies, including the first-
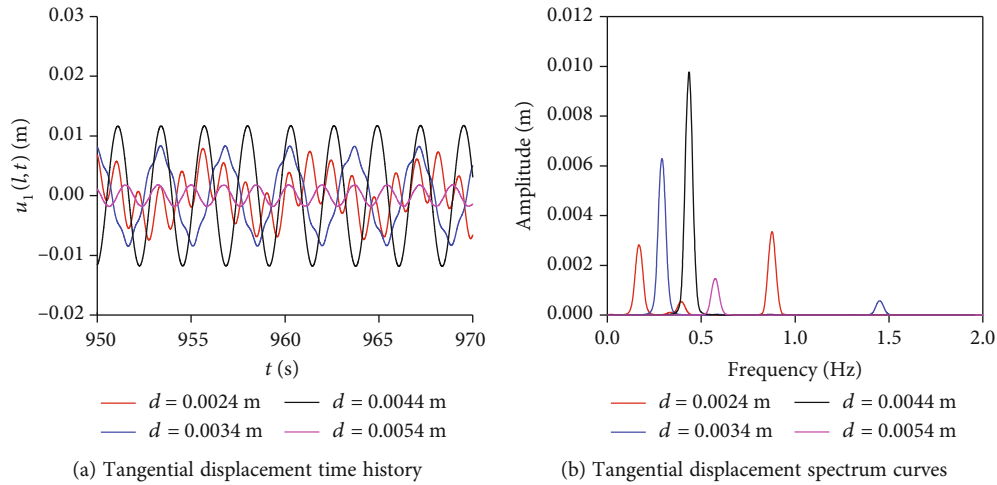
(a) Tangential displacement time history

(b) Tangential displacement spectrum curves

FIGURE 12: Tangential displacement time history and spectrum curves of the UAV under different cable diameters.

(a) Normal displacement time history
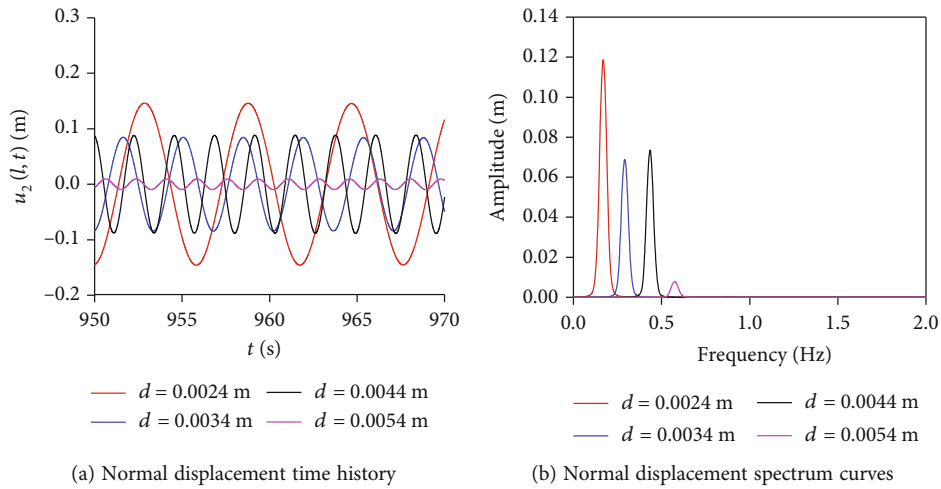

(b) Normal displacement spectrum curves

FIGURE 13: Normal displacement time history and spectrum curves of the UAV under different cable diameters.

order natural frequency of 0.292 Hz and the 5-fold frequency of 1.460 Hz, while the amplitude of the 5-fold frequency is 8.329% of that of the first-order natural frequency. When the cable diameter is 0.0044 m and 0.0054 m, the tangential motion of the UAV only has the first-order natural frequency of 0.434 Hz and 0.574 Hz, respectively. As the cable diameter increases, the natural frequency of the tangential motion of the UAV gradually increases, the frequency doubling component gradually decreases, and the UAV returns from the first two orders of motion to the first order of motion.

Besides, analyzing the normal displacement variation of the UAV in Figure 13(a) indicates that all the normal displacements have a periodic trend for different cable diameters. The UAV normal displacement spectrum curves in Figure 13(b) show that the UAV normal motion has the first-order natural frequencies of 0.174 Hz, 0.285 Hz, 0.436 Hz, and 0.579 Hz when the cable diameter is 0.0024 m, 0.0034 m, 0.0044 m, and 0.0054 m, respectively, indicating the first-order motion of the UAV. As the cable diameter increases, the natural frequency of the UAV also

increases gradually. This is because as the diameter of the cable increases, the wind load on it increases, increasing the static equilibrium tension of the cable and thereby increasing the natural frequency of the UAV.

(2) UAV Motion under Different Cable Diameters. The UAV motion under different cable diameters provides a theoretical reference for flight control design. Figure 14 shows the UAV displacement under different cable diameters by setting the cable diameter as 0.0014 m~0.0104 m. As shown in Figure 14, the UAV generates a complex bifurcation behavior under cable diameter variations. Figure 14(a) shows the tangential displacement of the UAV. When the cable diameter varies from 0.0014 m to 0.0024 m, multiple periodic solutions for the UAV motion can be found in region I. The UAV motion has one periodic solution in region II when the cable diameter varies from 0.0024 m to 0.0054 m. However, the local enlargement of Figure 14(b) shows that the UAV motion in region III again generates multiple periodic solutions when the cable diameter exceeds 0.0054 m.

(a) The tangential displacement of the UAV

(b) Local enlargement of (a)

(c) The normal displacement of the UAV
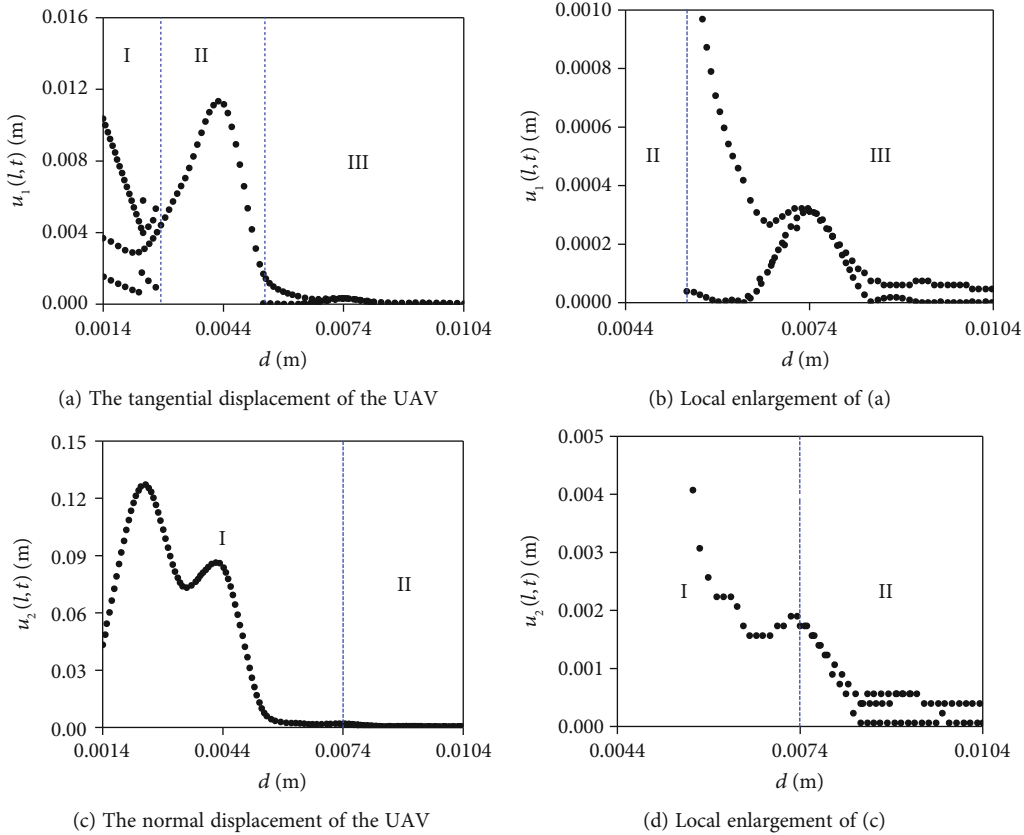
(d) Local enlargement of (c)

Figure 14: Displacement of UAV under different cable diameters.

This indicates that the UAV motion generates alternating multiperiodic and single-periodic solutions as the cable diameter increases.

Figure 14(c) shows the UAV normal displacement for the cable diameter varying from 0.0014 m to 0.0074 m. It can be seen that the UAV motion has only one periodic solution in region I. The local enlargement of Figure 14(d) indicates multiple periodic solutions for the UAV motion in region II when the cable diameter exceeds 0.0074 m.

Figure 15 shows the tangential and normal motion phase diagrams of the UAV for cable diameters of 0.0024 m in region I. The tangential phase trajectory curve comprises multiple limit loops, making the tangential motion of the UAV generate multiple periodic solutions and a multiperiodic motion. The normal phase trajectory curves form a single circular limit loop so that the normal motion of the UAV has only one periodic solution, and UAV exhibits a single-period stable motion.

3.2.3. Vibration Analysis of the System under Different Elastic Moduli of the Cable

(1) System Motion under Different Elastic Moduli of the Cable. The magnitude of the cable's elastic modulus plays a significant role in the cable tension, subsequently influencing the motion of the UAV. This elastic modulus is subject to variation based on the cable's structure and material composition. Drawing from engineering practice, four equivalent moduli of elasticity have been chosen, namely, 1.206×10^9 Pa, 1.426×10^9 Pa, 1.647×10^9 Pa, and 1.867×10^9 Pa. In order to verify the system vibration under different cable elastic moduli, the time history of tension at the upper endpoint of the cable, UAV's tangential and normal displacements when the cable elastic modulus is 1.206×10^9 Pa, 1.426×10^9 Pa, 1.647×10^9 Pa, and 1.867×10^9 Pa, and the spectrum curves obtained after applying the Fourier transform are plotted in Figures 16–18, respectively. The cable tension of Figure 16(a) shows a periodic motion. As shown in Figure 16(b), due to the coupling of cable tension and tangential motion, the frequency components of the cable tension are similar to those of the UAV tangential motion in Figure 17(b) for different cable elastic moduli. Besides, since the amplitude of the frequency doubling of the cable tension in each cable elastic modulus is much smaller than that of the fundamental frequency, the cable tension does not generate significant nonlinear characteristics.

As shown in Figure 17(a), the tangential displacement of the UAV shows a periodic motion. The frequency components of the tangential motion of the UAV in Figure 17(b) indicate a natural frequency and a frequency doubling component under different cable elastic moduli, where the natural frequencies are 0.237 Hz, 0.252 Hz, 0.277 Hz, and 0.292 Hz for the cable elastic moduli of 1.206×10^9 Pa,
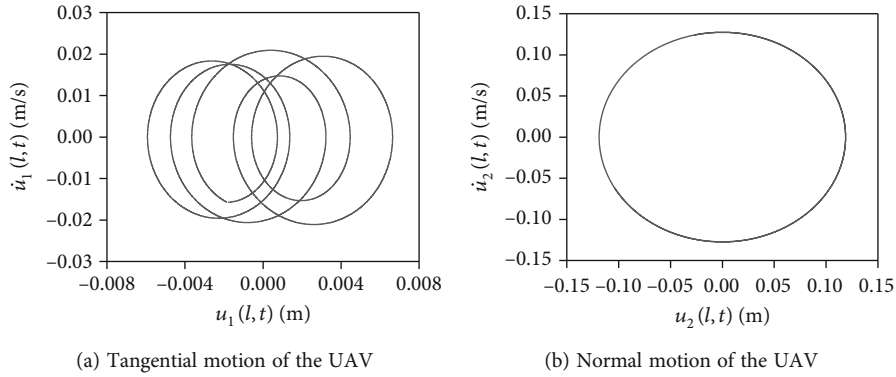
(a) Tangential motion of the UAV

(b) Normal motion of the UAV

Figure 15: UAV motion for $d = 0.0024$ m.

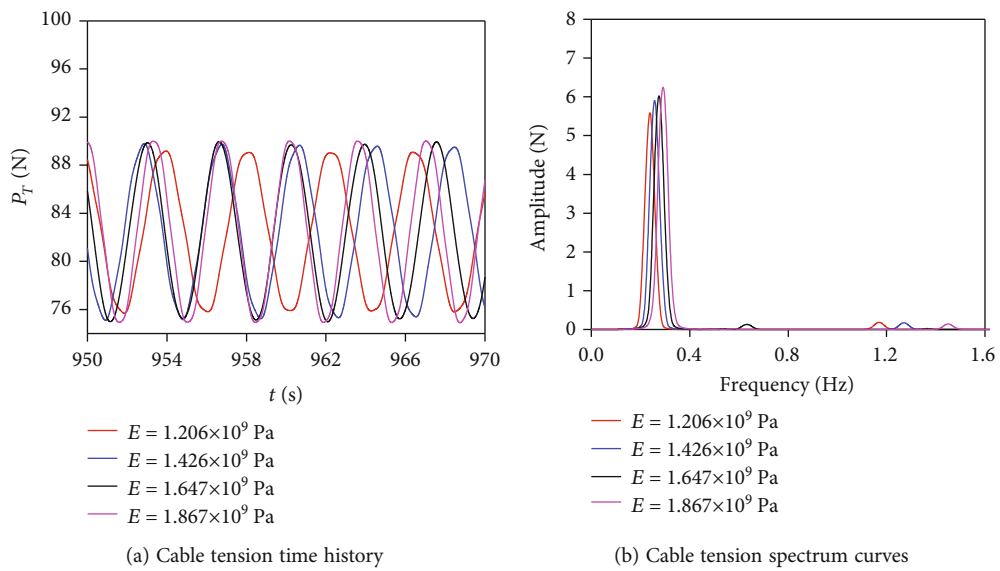(a) Cable tension time history

(b) Cable tension spectrum curves

Figure 16: Tension time history and spectrum curves of the upper end of cable under different elastic moduli.

(a) Tangential displacement time history

(b) Tangential displacement spectrum curves
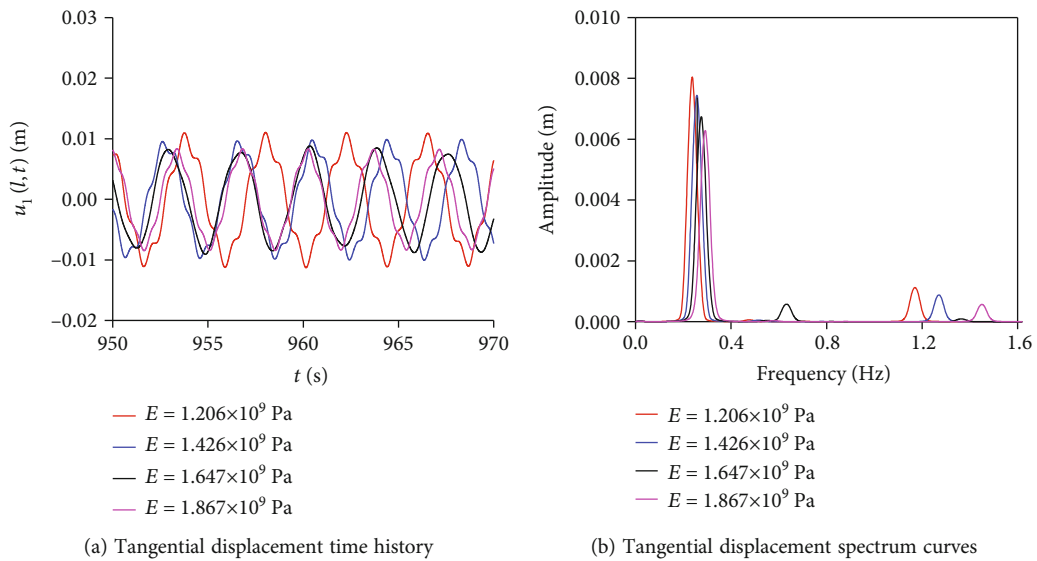
Figure 17: Tangential displacement time history and spectrum curves of the UAV under different cable elastic moduli.

(a) Normal displacement time history
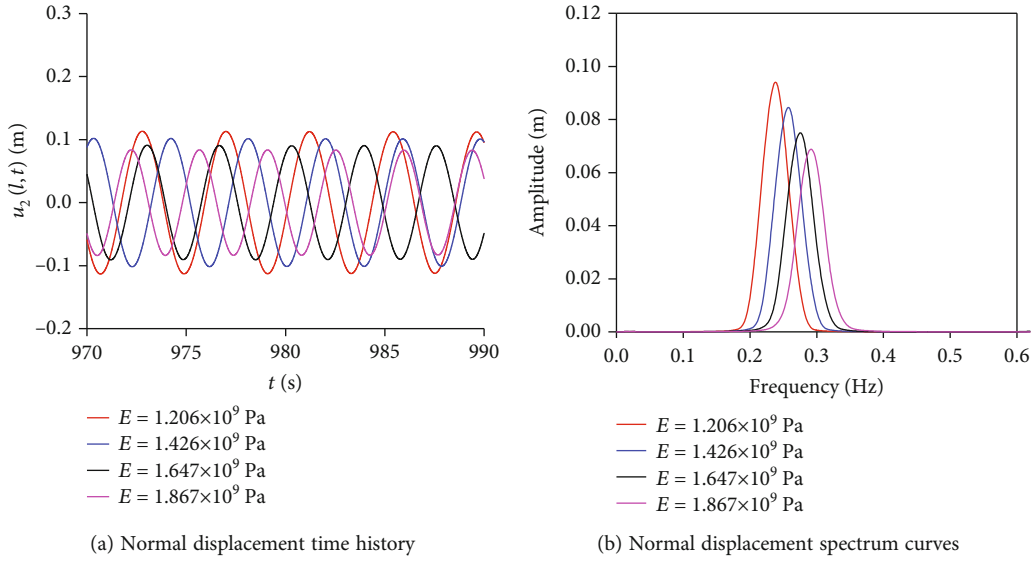

(b) Normal displacement spectrum curves

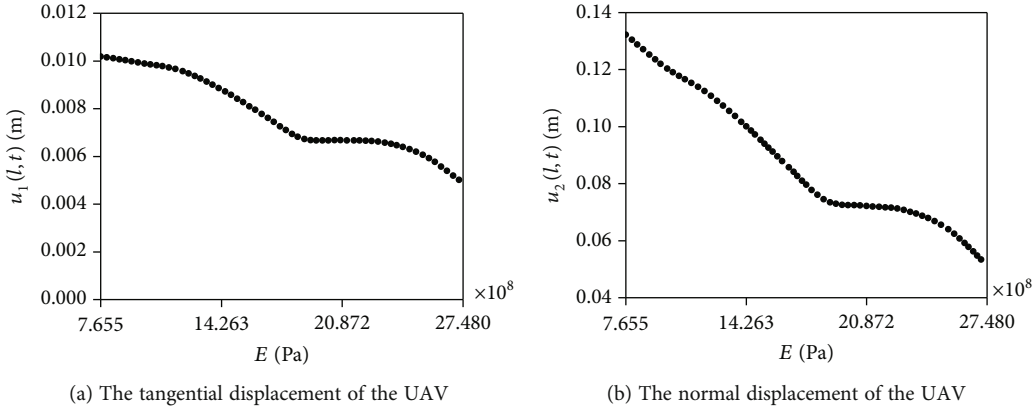FIGURE 18: Normal displacement time history and spectrum curves of the UAV under different cable elastic moduli.

(a) The tangential displacement of the UAV

(b) The normal displacement of the UAV

FIGURE 19: Displacements of the UAV under different cable elastic moduli.

1.426×10^9 Pa, 1.647×10^9 Pa, and 1.867×10^9 Pa, respectively. The above analysis demonstrates that the natural frequency of the tangential motion of the UAV gradually increases as the elastic modulus of the cable increases. This is due to the increase in cable stiffness, increasing the static equilibrium tension of the cable, thereby increasing the natural frequency of the UAV. Besides, the tangential amplitude of the UAV gradually decreases as the elastic modulus of the cable increases.

Furthermore, as shown in Figure 18(a), the normal displacement of the UAV has a periodic trend for different cable elastic moduli. The UAV's normal displacement spectrum curves in Figure 18(b) show that the natural frequencies of the UAV's normal motion are 0.241 Hz, 0.249 Hz, 0.282 Hz, and 0.292 Hz when the cable elastic moduli are 1.206×10^9 Pa, 1.426×10^9 Pa, 1.647×10^9 Pa, and 1.867×10^9 Pa, respectively. This indicates that the natural frequency of the normal motion of the UAV gradually increases as the cable elastic modulus increases. Besides, the normal amplitude of the UAV gradually decreases as the cable elastic modulus increases.

(2) UAV Motion under Different Cable Elastic Moduli. The motion of the UAV under different cable elastic moduli provides a theoretical reference for flight control design. Figure 19 shows the UAV displacements under different cable elastic moduli when the cable modulus of elasticity is set as 7.655×10^8 Pa ~ 27.480×10^8 Pa. Figures 19(a) and 19(b) indicate that the tangential and normal displacements of the UAV exhibit only one periodic solution in the whole range of the cable elastic modulus change.

Figure 20 shows the UAV's tangential and normal motion phase diagrams for the cable elastic modulus of 1.426×10^9 Pa. The tangential phase trajectory curve is a single irregular limit loop. The normal phase trajectory curve is a single-circular limit loop, and the UAV exhibits a single-period stable motion.

The above study indicates that the cable tension is mainly coupled with the tangential first-order motion of the UAV under the transient wind field, the UAV's nonlinear characteristics are more evident than the normal motion, and the focus should be on the tangential motion of the

(a) Tangential motion of the UAV
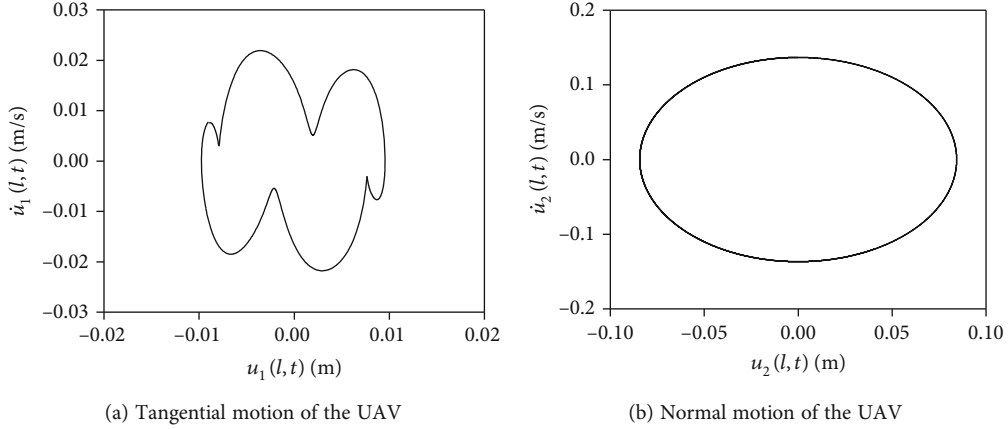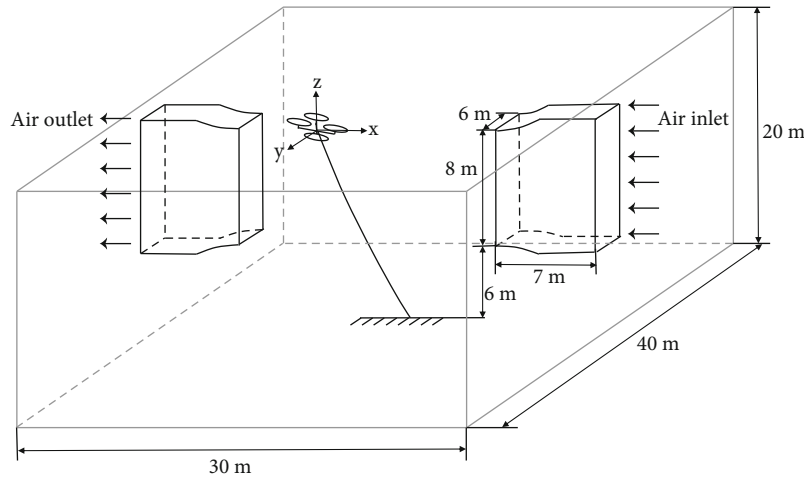
(b) Normal motion of the UAV

FIGURE 20: UAV motion for $E = 1.426 \times 10^9$ Pa.

FIGURE 21: Schematic diagram of the tethered UAV experimental site.

TABLE 2: The composite cable parameters.

Type	Length (m)	Diameter (mm)	Linear density (g/m)	Elastic modulus (N/m^2)
10 AWG	14	5.50	79.12	4.217×10^8

system when designing the flight control of the tethered UAV. Furthermore, when designing the tethered UAV structure, setting the parameters as $l > 141.055$ m, $E > 7.655 \times 10^8$ Pa, and 0.0024 m $< d < 0.0054$ m under the premise of actual demand allows the UAV to maintain a stable single-period motion.

4. Experimental Verifications

In order to evaluate the numerical method, an experiment on the vibration response of the tethered UAV system in a wind tunnel is conducted. The numerical and experimental results are compared to evaluate the correctness and accuracy of the theoretical method.

The experiment on the vibration response of the tethered UAV system is conducted in a wind tunnel laboratory. Figure 21 describes the coordinate system and experimental site. The tuyere is 8 m long and 6 m wide, the wind flows

through the middle experimental area, and the V_A and T are 6 m/s and 1 s, respectively. The lower edge of the wind tunnel, elevated 6 m from the ground, results in the generation of a wind speed that varies in relation to the height of the cable. This mechanism successfully replicates the wind speed gradient typically experienced in natural settings.

A quadrotor UAV produced by Guantong Yuntian Technology Co., Ltd. is selected as the test object, where its body weight is 4.9 kg, the expanded size is 1 m. Table 2 shows the composite cable parameters. According to the size of the wind tunnel and the UAV, the cable length is selected as 14 m to ensure that the UAV is within the tuyere range.

We use a DYMH-103 tension sensor, made by Bengbu Dayang Sensing System Engineering Co., Ltd., to gauge the tension at the cable's upper end, as illustrated in Figure 22(a). This tension sensor is linked with a dynamic test signal acquisition device, which collects and processes

(a) DYMH-103 tension sensor

(b) Dynamic test signal acquisition device

FIGURE 22: Experimental measurement equipment.

(a) Cable tension time history
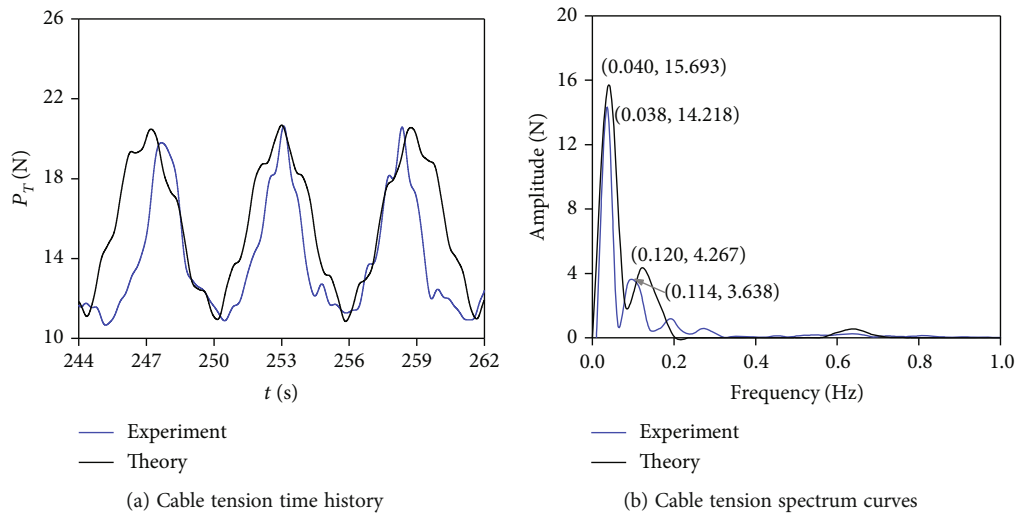

(b) Cable tension spectrum curves

FIGURE 23: The experimentally measured and simulated tensions.

the obtained tension data. The signal acquisition device, produced by Jiangsu Donghua Testing Technology Co., Ltd. and bearing the model number DH5922, is shown in Figure 22(b).

The accuracy of the theoretical method is substantiated by comparing the results derived from its application, based on the parameters of the experimental system, with the actual experimental results. The tension at the upper end is recorded and shown in Figure 23(a). The maximum and minimum tensions are 20.631 N and 10.657 N, respectively. The maximum and minimum tension values obtained with the numerical simulations with the same system parameters are 20.679 N and 10.846 N, respectively. It can be seen that both experimental and theoretical tensions have the same periodic motion. Besides, the errors between the experimental and theoretical values of maximum and minimum tensions are only 0.233% and 1.773%, respectively. Since the theoretical simulation in this paper neglects the cable damping, the theoretical tension is slightly larger than the experimental one [15].

In order to evaluate the consistency of the two frequency components, the Fourier transform is applied to the tension curves to obtain the spectrum curves, as shown in Figure 23(b). Both experimental and theoretical tensions have fundamental and frequency doubling component, which are 0.038 Hz, 0.114 Hz, 0.040 Hz, and 0.120 Hz, respectively, and errors between the experimental and theoretical values of the fundamental and frequency doubling component are only 5.263% and 5.263%, respectively. Overall, the above comparison indicates the correctness and accuracy of the theoretical method.

5. Conclusion

One of the major concerns faced by tethered UAVs operating over the ocean is the transient wind conditions. Nevertheless, there has been a scarcity of comprehensive research on the dynamics of tethered UAV systems under transient wind. With the aim of enhancing the applicability and understanding of tethered UAVs, this study primarily

concentrates on analyzing the vibration response of tethered UAVs under transient wind conditions. The outcomes of this analysis are outlined below:

(1) Considering both the motion of cable and UAV, a coupled dynamic model of the tethered UAV system is established using the Hamilton principle. The model is closer to reality and the calculated results are accurate

(2) As V_A and T change, the cable generates vibration amplitudes with equal size at different positions. According to the variation law of the cable amplitude with V_A, T, and s, the cable's dynamic behavior in the actual flight can be preliminarily evaluated and premeasured

(3) The positions of maximum vibration amplitude in tangential and normal directions are approximately 9/10 and 9/20 from the lower end of the cable

(4) Changing the parameter as $l > 141.055$ m, $E > 7.655 \times 10^8$ Pa, and 0.0024 m $< d < 0.0054$ m allows the UAV to maintain a stable single-period motion

(5) The UAV exhibits multiple periodic vibrations in the tangential direction; however, it exhibits single-periodic vibrations in the normal direction. The nonlinear characteristics of the tangential motion of the UAV are more obvious than the normal motion; it is necessary to focus on the tangential motion of the UAV when designing the flight control

Finally, in order to validate the numerical method, an experiment on the vibration response of the tethered UAV system is conducted in a wind tunnel. The numerical result is compatible with the experimental one, demonstrating the correctness and accuracy of the theoretical method. Overall, the findings of this study provide technical support and a reliable basis for formulating effective guidelines and boost the practical applications of tethered UAVs.

6. Engineering Suggestions

We have investigated the vibration response of a tethered UAV under different wind field parameters and structural parameters. According to the study results, three engineering suggestions are provided for tethered UAVs. (1) The positions of maximum amplitude of the cable obtained in this paper can be used to reduce system vibration. (2) The laws of system vibration with structural parameters given in this paper can be used to guide the selection of structural parameters in the design of tethered UAVs to ensure that the UAV maintains a stable single-period motion, which helps with the flight control. (3) The cable gradually elongates as the UAV flies up in practice. The flight control needs to focus on the motion of the UAV in the direction of cable elongation, i.e., the tangential motion of the UAV.

Data Availability

Data used to support the findings of this study are available from the corresponding author upon request.

Conflicts of Interest

The authors declare that there is no conflict of interest regarding the publication of this paper.

Acknowledgments

References

[1] Y. Dai, Y. Yuan, S. Song, and Y. Li, "Steady–state and transient wind characteristics of low–rise building roofs with openings in vulnerable areas," *Advances in Structural Engineering*, vol. 23, no. 11, pp. 2343–2357, 2020.

[2] G. Kristóf, B. Papp, H. Wang, and J. Hang, "Investigation of the flow and dispersion characteristics of repeated orographic structures by assuming transient wind forcing," *Journal of Wind Engineering and Industrial Aerodynamics*, vol. 197, article 104087, 2020.

[3] Z. Li, C. Yang, and Y. Zhu, "Research on sliding mode control algorithm for tethered quadrotor UAV," *Electronic Design Engineering*, vol. 26, no. 3, pp. 160–169, 2018.

[4] F. Muttin, "Umbilical deployment modeling for tethered UAV detecting oil pollution from ship," *Applied Ocean research*, vol. 33, no. 4, pp. 332–343, 2011.

[5] Q. L. Xie, *Research on Control Algorithm for Tethered Unmanned Tethered Quadrotor Helicopter, [M.S. Thesis]*, Shenyang Aerospace University, China, 2014.

[6] J. T. Mfiri, J. A. A. Treurnicht, and J. Engelbrecht, "Automated landing of a tethered quad–rotor UAV with constant winching force," in *2016 Pattern Recognition Association of South Africa and Robotics and Mechatronics International Conference (PRASA-RobMech)*, pp. 1–6, Stellenbosch, South Africa, 2016.

[7] S. Eeckhout, M. Nicotra, R. Naldi, and E. Garone, "Nonlinear control of an actuated tethered airfoil," in *22nd Mediterranean Conference on Control and Automation*, pp. 1412–1417, Palermo, Italy, 2014.

[8] T. W. Nguyen, M. M. Nicotra, and E. Garone, "Geodesic approach for the control of tethered quadrotors," *Journal of Guidance, Control, and Dynamics*, vol. 43, no. 4, pp. 854–862, 2020.

[9] E. Rossi, M. Bruschetta, R. Carli, Y. Chen, and M. Farina, "Online nonlinear model predictive control for tethered UAVs to perform a safe and constrained maneuver," in *2019 18th European Control Conference (ECC)*, pp. 3996–4001, Naples, Italy, 2019.

[10] Y. Wang, Q. Li, C. Wang, J. Zhu, and X. Wang, "Tethered UAVs based applications in emergency surveying and mapping," *Remote Sensing for Land and Resources*, vol. 32, no. 1, pp. 1–6, 2020.

[11] X. B. Li, Z. R. Peng, Q. C. Lu et al., "Evaluation of unmanned aerial system in measuring lower tropospheric ozone and fine aerosol particles using portable monitors," *Atmospheric Environment*, vol. 222, article 117134, 2020.

[12] W. Wang, *Research on Establishment of Space–Air–Ground Integrated Monitoring Technology System for Air Pollution, [M.S. Thesis]*, Chongqing Technology and Business University, China, 2020.

[13] S. Yang and H. Sui, "Design and application of high altitude base station communication system based on tethered UAV," *Electronics World*, vol. 16, pp. 136-137, 2020.

[14] H. Li and L. Wang, "Dynamic simulation analysis of wind-resistant performance for a tethered balloon," *Journal of Astronautic Metrology and Measurement*, vol. 34, no. 6, pp. 29–32, 2014.

[15] G. S. Aglietti, "Dynamic response of a high–altitude tethered balloon system," *Journal of Aircraft*, vol. 46, no. 6, pp. 2032–2040, 2009.

[16] S. Redi, G. S. Aglietti, A. R. Tatnall, and T. Markvart, "Dynamic response to turbulence of tethered lighter–than–air platforms," *Journal of Aircraft*, vol. 48, no. 2, pp. 540–552, 2011.

[17] W. Kang and I. Lee, "Analysis of tethered aerostat response under atmospheric turbulence considering nonlinear cable dynamics," *Journal of Aircraft*, vol. 46, no. 1, pp. 343–348, 2009.

[18] W. J. Kim and N. C. Perkins, "Linear vibration characteristics of cable–buoy system," *Journal of Sound and Vibration*, vol. 252, no. 3, pp. 443–456, 2002.

[19] A. D. Freed, S. Zamani, L. Szabo, and J. D. Clayton, "Laplace stretch: Eulerian and Lagrangian formulations," *Zeitschrift für angewandte Mathematik und Physik*, vol. 71, no. 5, 2020.

[20] S. Cao and M. Li, "Numerical study of flow over a circular cylinder in oscillatory flows with zero-mean and non-zero-mean velocities," *Journal of Wind Engineering and Industrial Aerodynamics*, vol. 144, pp. 42–52, 2015.

[21] N. C. Perkins and C. D. Mote Jr., "Three-dimensional vibration of travelling elastic cables," *Journal of Sound and Vibration*, vol. 114, no. 2, pp. 325–340, 1987.

[22] W. S. Nie, X. K. Che, and H. B. He, *Aerodynamics Research and Experimental Techniques*, National Defense Industry Press, Beijing, China, 2018.

[23] M. H. Zhao, X. Y. Liu, Y. S. Chang, and Q. J. Chen, "Force simulation analysis of underground quadrotor UAV based on virtual laboratory technology," in *2021 6th Asia-Pacific Conference on Intelligent Robot Systems (ACIRS)*, pp. 1–4, Tokyo, Japan, 2021.

[24] Y. Chen, Y. He, and M. Zhou, "Decentralized PID neural network control for a quadrotor helicopter subjected to wind disturbance," *Journal of Central South University*, vol. 22, no. 1, pp. 168–179, 2015.

[25] L. Muñoz, O. Santos, and P. C. Garcia, "Nonlinear and robust control strategy to stabilize in real time a PVTOL aircraft exposed to crosswind," in *2010 IEEE/RSJ International Conference on Intelligent Robots and Systems*, Taipei, China, 2010.

[26] W. J. Kim and N. C. Perkins, "Coupled slow and fast dynamics of flow excited elastic cable systems," *Journal of Vibration & Acoustics*, vol. 125, no. 2, pp. 155–161, 2003.

[27] A. Luongo, D. Zulli, and G. Piccardo, "A linear curved–beam model for the analysis of galloping in suspended cables," *Journal of Mechanics of Materials and Structures*, vol. 2, no. 4, pp. 675–694, 2007.

[28] A. Q. Zhou, X. J. Liu, S. X. Zhang, F. Cui, and P. Liu, "Wind tunnel test of the influence of an interphase spacer on the galloping control of iced eight-bundled conductors," *Cold Regions Science and Technology*, vol. 155, pp. 354–366, 2018.

[29] X. G. Dong, X. X. Meng, H. X. Xu, Y. C. Chen, and H. B. Liu, "WRF 3DVAR data assimilation numerical simulation and analysis of wind energy resources over Bohai Sea region," *Journal of Natural Resources*, vol. 29, no. 6, pp. 1029–1042, 2014.

[30] W. L. Wang, *Atmospheric Wind Field Modeling and Its Application, [M.S. Thesis]*, National University of Defense Technology, China, 2009.

[31] P. Si, N. N. Zhu, H. Su, and D. P. Liang, "Operational evaluation and wind speed data quality check of a station on Suizhong 36 offshore oil platform," *Ocean Forecasts*, vol. 36, no. 1, pp. 27–36, 2019.

[32] P. G. Ioppo, *The Design, Modelling and Control of an Autonomous Tethered Multirotor UAV, [Ph.D. Thesis]*, University of Stellenbosch, South Africa, 2017.